Two-Dimensional Modelling for Catalytically Stabilized Combustion of a Lean Methane-Air Mixture With Elementary Homogeneous and Heterogeneous Chemical Reactions

URS DOGWILER,* PETER BENZ, AND JOHN MANTZARAS
Paul Scherrer Institute, Combustion Research, CH-5232 Villigen-PSI, Switzerland

The catalytically stabilized combustion (CST) of a lean (equivalence ratio $\Phi = 0.4$) methane-air mixture was investigated numerically in a laminar channel flow configuration established between two platinum-coated parallel plates 50 mm long and 2 mm apart. A two-dimensional elliptic fluid mechanical model was used, which included elementary reactions for both gaseous and surface chemistry. Heat conduction in the solid plates and radiative heat transfer from the hot catalytic surfaces were accounted for in the model. Heterogeneous ignition occurs just downstream of the channel entrance, at a streamwise distance (x) of 4 mm. Sensitivity analysis shows that key surface reactions influencing heterogeneous ignition are the adsorption of CH_4 and O_2 and the recombinative desorption of surface-bound O radicals; the adsorption or desorption of radicals other than O has no effect on the heterogeneous ignition location and the concentrations of major species around it. Homogeneous ignition takes place at $x = 41$ mm. Sensitivity analysis shows that key surface reactions controlling homogeneous ignition are the adsorption/desorption of the OH radical and the adsorption/desorption of H_2O, the latter due to its direct influence on the OH production path. In addition, the slope of the OH lateral wall gradient changes from negative (net-desorptive) to positive (net-adsorptive) well before homogeneous ignition ($x = 30$ mm), thus exemplifying the importance of a detailed surface chemistry scheme in accurately predicting the homogeneous ignition location. The effect of product formation on homogeneous ignition was studied by varying the third body efficiency of H_2O. Product formation promotes homogeneous ignition due to a shift in the relative importance of the reactions $H + O_2 + M \rightarrow HO_2 + M$ and $HCO + M \rightarrow CO + H + M$. © 1998 by The Combustion Institute

INTRODUCTION

In catalytically stabilized thermal combustion (CST) a catalyst acts to initiate and stabilize homogeneous gaseous combustion via thermal and chemical interactions with heterogeneous exothermic surface oxidation reactions. CST has received increased interest over the last years for its potential to expand the lean stability limit and achieve ultralow emissions (of nitrogen oxides and products of incomplete combustion) in practical combustors such as stationary gas turbines, industrial boilers, or household burners. Following the initial demonstration of CST by Pfefferle [1], substantial theoretical and experimental work was undertaken in this field. The interdisciplinary nature of CST has called for improvement of our knowledge of the coupling between catalyst performance, surface kinetics, fluid mechanical transport, and low temperature gas phase combustion.

In parallel with surface kinetics studies of fuels such as H_2, CO, and CH_4 over Pt and Pd catalysts [2–4] major efforts have been directed to the numerical investigation of the coupling between heterogeneous and homogeneous gas phase reactions in simple laminar, one- and two-dimensional flow configurations over catalytically active surfaces. Such simulations include one-dimensional stagnation point flows [5, 6], two-dimensional parabolic (boundary layer) flows [7, 8], and two-dimensional elliptic channel flows [9, 10]; all of these used detailed gas phase chemistry and, at least for the two-dimensional cases, either a mass-transport limited global reaction or simplified surface kinetics. Fundamental questions addressed in the previous as well as other similar studies were ignition and extinction (blowout) characteristics of CST as a function of fuel type and equivalence ratio, wall temperature, inlet reactant velocity and temperature, and catalyst activity [6–14]; identification of the regimes of catalytic combustion (heterogeneous vs homogeneous reactions and inhibition of one path over the other) [5]; Lewis number effects of diffusionally

*Corresponding author.

COMBUSTION AND FLAME 116:243–258 (1999)
© 1998 by The Combustion Institute
Published by Elsevier Science Inc.
0010-2180/99/$19.00
PII S0010-2180(98)00036-4

imbalanced mixtures on catalyst wall temperatures [10–12]; and effect of catalytic fuel conversion on combustion efficiency and pollutant (NO_x) reduction [15, 16].

Catalytic combustors, such as those used in natural gas fired turbines, are usually made of a catalytically active monolith-bed consisting of a multitude of tubular channels. To prevent the formation of hot spots, provision is made to assure nearly identical operating conditions in each channel. Understanding the combustion in such a burner requires modeling of the processes occurring in each individual channel. The channel cross section can be circular, triangular, or square, so at least a two-dimensional model is required. In most practical applications the incoming velocity and scalar profiles are uniform at the channel entrance and hence an elliptic fluid mechanical description is best suited to properly account for the leading edge effects where the boundary layer approximation breaks down. Gaseous flame propagation can also invalidate the boundary layer approximation if followed by a strong volumetric expansion. As detailed surface mechanisms for fuel oxidation over Pt or Pd catalysts have become available in the last years, their application in conjunction with full gaseous chemistry is crucial to an understanding of the coupling between homogeneous gas phase and surface chemistry. In particular, issues such as the effect of radical (OH, O, and H) adsorption or desorption on gas phase ignition and stabilization can be only accounted with complete gas and surface chemistry. No study in CST has yet attempted to include detailed gas phase and surface chemistry schemes coupled to a two-dimensional elliptic fluid mechanical description.

In this article we develop, for the first time, a detailed numerical model for CST of lean CH_4-air mixtures in channels coated with technical (Pt/Al_2O_3) catalysts. Elementary gaseous and surface chemistries are considered along with a laminar, elliptic, two-dimensional fluid mechanical model with molecular transport that includes thermal diffusion. Heat conduction inside the catalytic plates, an effect of prime importance for heterogeneous ignition, as well as radiative heat transfer from the hot catalyst surfaces are accounted for. The main objective of this study is to examine the coupling between heterogeneous and homogeneous reactions under operating conditions pertinent to technical applications. Of particular interest is the identification through sensitivity analysis of the key surface reactions affecting homogeneous ignition; the effect of radical adsorption/desorption and product formation on homogeneous ignition are examined in detail given the complete surface chemistry model description. The key surface reactions controlling heterogeneous ignition are also examined by performing a similar sensitivity analysis.

First the geometric and flow conditions of the simulation are given, the mathematical model along with the solution procedure follows, and then results are presented for the combustion processes with the order they physically occur in the channel: initially heterogeneous ignition is studied, then the processes leading to and including homogeneous ignition, and finally the homogeneous combustion propagation inside the channel.

BURNER GEOMETRY AND FLOW CONDITIONS

Figure 1a shows a typical honeycomb monolith composed of a large number of catalytically active square channels through which the gaseous premixture flows. Figure 1b presents the two-dimensional configuration employed in this study to simulate the combustion processes of each channel. It consists of two horizontal plates of thickness (δ_w) 0.4 mm, a vertical separation (H) of 2 mm, and a length (L) of 50 mm. This geometry is considered to capture the key processes occurring in a square channel of the same length and of 4 mm $\times$ 4 mm cross section, as they both have the same surface to volume ratio. The inner horizontal channel surfaces contain Pt on a Al_2O_3 washcoat. The site density (Γ) for this technical catalyst was taken as 2.7×10^{-9} moles/cm^2, as in Bond et al. [17]. One-dimensional heat conduction in the solid plates (crucial for the onset of heterogeneous ignition) was considered; the thermal conductivity (k_c) of the solid plates was taken as 1 W/mK, corresponding to a typical cordierite support material. Adiabaticity is imposed at the outer horizontal plate surfaces, a condition dictated by the

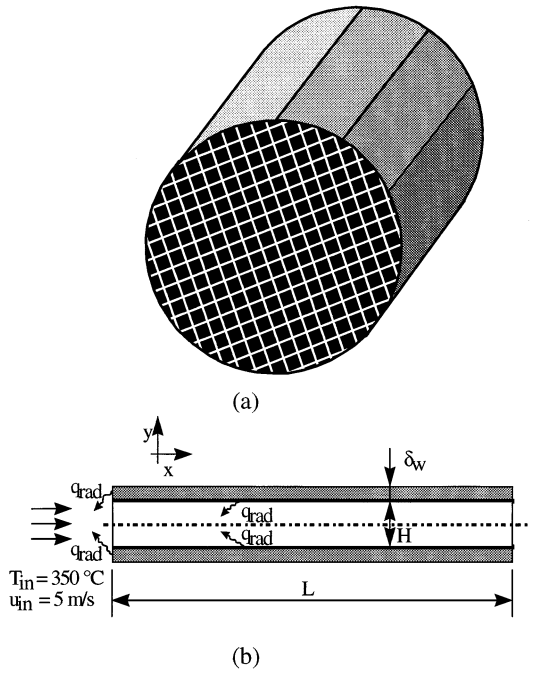

Fig. 1. (a) Typical honeycomb monolith catalytic combustor, (b) Geometry used to simulate an individual channel of the combustor.

requirement of identical operation between adjacent channels. Radiative heat transfer from the hot catalytic surfaces as well as from the vertical facets of the plates was also included with a corresponding emissivity of one (black body assumption).

The incoming CH_4-air flow was fully premixed with an equivalence ratio (Φ) of 0.4; it had a uniform inlet temperature (T_{IN}) of 350°C and a uniform axial velocity (U_{IN}) of 5 m/sec. The pressure was atmospheric and the Reynolds number based on the incoming properties was 360. The adiabatic flame temperature of the mixture was 1276°C. The very lean condition of this work, apart from its technical interest, aids in assessing the importance of the surface reactions as the gas phase reactivity is reduced.

NUMERICAL MODEL

Governing equations

The governing equations for a steady, laminar, two-dimensional reactive flow with surface reactions are as follows:

Continuity equation:

$$\frac{\partial(\rho u)}{\partial x} + \frac{\partial(\rho v)}{\partial y} = 0, \tag{1}$$

Momentum equations:

$$\frac{\partial(\rho u u)}{\partial x} + \frac{\partial(\rho v u)}{\partial y} + \frac{\partial p}{\partial x} - \frac{\partial}{\partial x} \cdot \left[2\mu \frac{\partial u}{\partial x} - \frac{2}{3}\mu\left(\frac{\partial u}{\partial x} + \frac{\partial v}{\partial y}\right)\right] - \frac{\partial}{\partial y}\left[\mu\left(\frac{\partial u}{\partial y} + \frac{\partial v}{\partial x}\right)\right] = 0, \tag{2}$$

$$\frac{\partial(\rho u v)}{\partial x} + \frac{\partial(\rho v v)}{\partial y} + \frac{\partial p}{\partial y} - \frac{\partial}{\partial x}\left[\mu\left(\frac{\partial v}{\partial x} + \frac{\partial u}{\partial y}\right)\right] - \frac{\partial}{\partial y}\left[2\mu \frac{\partial v}{\partial y} - \frac{2}{3}\mu\left(\frac{\partial u}{\partial x} + \frac{\partial v}{\partial y}\right)\right] + \rho g = 0, \tag{3}$$

Energy equation:

$$\frac{\partial(\rho u h)}{\partial x} + \frac{\partial(\rho v h)}{\partial y} + \frac{\partial}{\partial x} \cdot \left(\rho \sum_{k=1}^{K_g} Y_k h_k V_{k,x} - \lambda \frac{\partial T}{\partial x}\right) + \frac{\partial}{\partial y}\left(\rho \sum_{k=1}^{K_g} Y_k h_k V_{k,y} - \lambda \frac{\partial T}{\partial y}\right) = 0, \tag{4}$$

Gas phase species equations:

$$\frac{\partial(\rho u Y_k)}{\partial x} + \frac{\partial(\rho v Y_k)}{\partial y} + \frac{\partial}{\partial x}(\rho Y_k V_{k,x}) + \frac{\partial}{\partial y}(\rho Y_k V_{k,y}) - \dot{w}_k W_k = 0, \tag{5}$$

$$k = 1, 2, \ldots K_g - 1,$$

and for the carrier nitrogen,

$$Y_{N_2} = 1 - \sum_{k=1}^{K_g - 1} Y_k$$

Surface species coverage equations

$$\frac{\partial \Theta_m}{\partial t} = \sigma_m \frac{\dot{s}_m}{\Gamma} - \frac{\Theta m}{\Gamma} \dot{\Gamma}, \qquad (6)$$

$$m = 1, 2, \ldots M_s - 1,$$

and for the last surface coverage

$$\Theta_{M_s} = 1 - \sum_{m=1}^{M_s - 1} \Theta_m$$

In the above equations x and y are the spatial coordinates parallel and perpendicular to the surface, u and v the corresponding velocity components, g is the gravitational acceleration, λ and μ are the thermal conductivity and viscosity of the mixture respectively, p is the pressure, ρ is the gas density, T is the temperature, h is the total enthalpy of the mixture, Y_k, $\dot{w}_k$, W_k, and h_k are the mass fraction, molar production rate, molecular weight, and total enthalpy of the kth gas phase species respectively, K_g is the total number of gas phase species, and $V_{k,x}$, $V_{k,y}$ are the x- and y-components of the kth species diffusion velocity. Finally, Θ_m, σ_m, and $\dot{s}_m$ denote the coverage, the number of occupied surface sites, and the molar production rate of the mth surface species, respectively; the total number of surface species is M_s. The left side of Eq. 6 is not a true transient term and has been only introduced to facilitate convergence to steady state, as will be discussed in the solution algorithm section. For a surface reaction scheme that conserves the total number of sites, as used in this study, the second term on the right side of Eq. 6 is identically zero. The diffusion velocity vector $\vec{V}_k(V_{k,x}, V_{k,y})$ includes thermal diffusion for the light species and is defined as

$$\vec{V}_k = -D_k \vec{\nabla}[\ln(Y_k \bar{W}/W_k)] + [D_k \theta_{T,k} W_k/(Y_k \bar{W})]\vec{\nabla}(\ln T), \qquad (7)$$

where D_k and $\theta_{T,k}$ are the mixture diffusion coefficient and the thermal diffusion ratio [18] of the kth species, respectively, and $\bar{W}$ is the mixture average molecular weight. Finally, the ideal gas and caloric equations of state are

$$p = \rho RT/\bar{W}, \qquad (8)$$

$$h_k = h_k^0(T_0) + \int_{T_0}^{T} c_{p,k}\, \mathrm{d}T \qquad (9)$$

with $T_0 = 298$ K and R the universal gas constant. The first and second terms on the right of Eq. 9 are the chemical and sensible energies of species k, respectively, and $c_{p,k}$ is its heat capacity at constant pressure. The set of Eqs. (1–6) supplemented with the auxiliary relations (7–9) are solved for u, v, ρ, T, (Y_k, $k = 1, 2, \ldots K_g$), and (Θ_m, $m = 1, 2, \ldots M_s$).

Boundary Conditions

The interfacial energy boundary condition is

$$\dot{q}_r + \frac{\mathrm{d}\dot{q}_c}{\mathrm{d}x}\delta_w - \lambda_+ \left(\frac{\partial T}{\partial y}\right)_+ + \rho_+ \sum_{k=1}^{K_g} (Y_k h_k V_{k,y})_+ = 0 \qquad (10)$$

with $\dot{q}_r$ the surface radiation and $\dot{q}_c$ the one-dimensional heat conduction in the solid plate. The subscript (+) indicates gas phase properties at the gas-wall interface. The interfacial boundary conditions for the gas phase species are

$$(\rho Y_k V_{k,y})_+ + \dot{s}_k W_k = 0, \qquad (11)$$

$$k = 1, 2, \ldots K_g$$

with $\dot{s}_k$ the net molar production rate of gas phase species k via adsorption-desorption heterogeneous reactions. The boundary conditions at the vertical faces of each catalyst plate are as follows:

$$k_c \left.\frac{\partial T_w}{\partial x}\right|_{x=0} = \sigma(T_{W,0}^4 - T'^4) \qquad \text{at } x = 0 \text{ and}$$

$$-k_c \left.\frac{\partial T_w}{\partial x}\right|_{x=L} = \sigma(T_{W,L}^4 - T_{L,m}^4) \qquad \text{at } x = L, \qquad (12)$$

where $T_{w,0}$ and $T_{w,L}$ are the wall temperatures at $x = 0$ and $x = L$, respectively, σ is the Stefan-Boltzmann constant, and $T_{L,m}$ is the average outlet gas temperature. In many practical applications metal holders are placed upstream of the entrance to straighten the flow. These components are heated by the combined radiative heat flux ($\dot{q}_{R,IN}$) from the catalytic

surfaces and the vertical plate faces. Assuming that the entire amount of $\dot{q}_{R,IN}$ is subsequently transferred convectively from the metal holder to the gas mixture, the gas temperature just downstream of the metal holder is $T' = T_{IN} + \dot{q}_{R,IN}/(\dot{m}\bar{c}_p)$, with $\dot{m}$ the incoming mass flux, and $\bar{c}_p$ the average inlet mixture heat capacity at constant pressure. The radiative preheat resulted in a 19 K temperature rise of the incoming mixture and was included to facilitate forthcoming experiments with such an inlet holder. In the radiation exchange computations the surrounding inlet (metal holder) and outlet surfaces are considered to be at thermal equilibrium with the corresponding gas temperatures (T' and $T_{L,m}$ respectively). Finally, zero gradient Neumann boundary conditions are used at the outlet for all gas phase variables and the no-slip condition at the wall for both velocity components. Implications of the Neumann outflow conditions are discussed in the results section.

Surface Chemistry Modelling

Gas phase species adsorption rates are described in terms of a sticking coefficient γ_k; the probability that a collision of the particular species k with the surface will result in adsorption. To convert sticking coefficients to the usual mass-action kinetic rate constants, the relation currently used in the combustion literature [19] is

$$k_{ads,k} = \left(\frac{1}{1 - \frac{\gamma_k}{2}}\right) \frac{\gamma_k}{\Gamma^m} \sqrt{\frac{RT}{2\pi W_k}} \tag{13}$$

with m the sum of all of the surface reactants' stoichiometric coefficients. We have recently [20] proposed a correction to the previous relation, for the following reasons. Equation 13 originated from kinetic theory considerations:

$$k_{ads,k} = \frac{\gamma_k}{\Gamma^m} \sqrt{\frac{RT}{2\pi W_k}} \tag{14}$$

with the square root term denoting the collisional frequency. When the sticking coefficient is large, however, the molecules have a high probability of attaching to the surface, resulting in a non-Maxwellian velocity distribution which alters the species flux to the surface. Motz and Wise [21] examined this effect for a surface covered only with free sites and derived the correction factor $1/(1 - \gamma_k/2)$ appearing henceforth in the brackets of Eq. 13. This correction factor, however, cannot account for partially or fully occupied surface sites. Under these conditions the correct correction factor should be $1/(1 - \gamma_k\Theta_{free}/2)$, and hence the adsorption rate constant becomes

$$k_{ads,k} = \left(\frac{1}{1 - \frac{\gamma_k\Theta_{free}}{2}}\right) \frac{\gamma_k}{\Gamma^m} \sqrt{\frac{RT}{2\pi W_k}}. \tag{15}$$

The necessity for the new correction factor is seen from the following example: if the sticking coefficient is unity but all surface sites are occupied ($\Theta_{free} = 0$), no adsorption takes place, the velocity distribution is still Maxwellian, and hence the correction factor must be one. This value is recovered with the newly proposed correction formula, whereas the old correction formula yields the erroneous value of two. The error in the application of Eq. 13 can be important in kinetically-controlled adsorption reactions involving species with large sticking coefficients and surfaces with low free-site availability ($\gamma \to 1$, $\Theta_{free} \to 0$). Such conditions can be encountered, for example, during the heterogeneous ignition of lean CO-air mixtures over Pt surfaces, as the sticking coefficient of CO is 0.84 [22] and the free platinum coverage drops well before the ignition point to values typically less than 0.1.

Solution Algorithm

The governing equations for the gas phase variables were solved using a finite volume approach. An orthogonal staggered grid of 70×25 points (x and y directions respectively) was used with variable grid spacing in both directions. Simulations were also performed with higher resolution (100×50) to assure grid independent solution. The entire height of the channel was included in the computational domain to account for possible asymmetries due to the presence of gravity in the y-momentum equation. The system of algebraic discretized

equations for the gas phase unknowns was solved iteratively using an ADI algorithm [23]. The starting wall temperature profile was 1400K so that a converged solution in the upper, vigorously burning branch of the heterogeneous ignition S-curve could be obtained. Surface coverages are coupled to the gas phase variables via the interfacial boundary conditions. A time-splitting was introduced between gas phase and surface coverage computations. After a step for all gas phase variables was completed, the surface coverages (Eq. 6) were solved for every wall element using a modified Newton method [24]; quasi-steady state solutions provided the new coverage of surface species. These in turn determined the new gas phase concentrations at the gas-wall interface. A few iterations were required to achieve surface coverages and gas concentrations at the wall that satisfied the species boundary conditions (Eq. 11). The entire procedure was repeated until convergence was achieved. The radiative heat exchange of each catalytic surface element with the opposed surface elements and the inlet and outlet surroundings was modelled using a network analysis [25]. When both the gas and surface chemistry mechanisms (described in the next section) were implemented, the computational time was 8 hr on a Sun ultra-1 workstation. With only the surface mechanism present, the corresponding time was 3 hr.

CHEMICAL KINETICS

For gaseous chemistry the C/H/O mechanism of Warnatz [26] was employed. Only C_1 chemistry was considered, a reasonable simplification for the very lean condition of this study. In total 100 reactions (46 reversible and 8 irreversible) and 16 species (excluding the carrier nitrogen) were included. For surface chemistry, the reaction mechanism by Deutschmann et al. [22] was used, which included 26 reactions, 7 gaseous species, and 10 surface species (excluding Pt). To facilitate the ensuing discussion the surface mechanism is given in Table 1. The thermochemical data needed to calculate the equilibrium constants for the three reversible reactions of Table 1 were taken from Warnatz et al. [27]. Finally, the Chemkin data base was used to evaluate transport and thermodynamic properties in the gas phase.

RESULTS AND DISCUSSION

Results are presented for two cases further denoted as *SG* and *S*. In *SG* both surface and gaseous chemistries are present, while in *S* the gaseous chemistry is turned off. Following the notation of Table 1, all species followed by (s) indicate surface-bound species. The inlet boundary conditions for the radical species OH, O, and H were uniform mass fractions, each equal to the small value of 10^{-15}. The computations show the influence of gravity to be minimal, resulting in a nearly symmetric solution. Hence, streamwise (x) profiles of surface-bound variables are presented for one surface only and lateral (y) profiles are given over half the channel height.

Heterogeneous Ignition

The heterogeneous ignition is identified with the aid of streamwise profiles of catalytic fuel conversion rates, wall temperatures, and wall concentrations. Figure 2 presents the local streamwise heterogeneous CH_4 mass conversion rate for both *SG* and *S*. Figure 3 shows streamwise profiles of the CH_4 mass fraction and Fig. 4 profiles for the O_2 mass fraction and temperature; wall profiles as well as profiles averaged over the channel cross section are given. The *SG* and *S* profiles of Figs. 2 to 4 essentially collapse to each other before and well after heterogeneous ignition and the following discussion on the heterogeneous ignition location applies to either *S* or *SG*. Owing to heat conduction in the solid plates the heterogeneous ignition is not manifested by an abrupt wall temperature rise. The approximate location of heterogeneous ignition is $x = 4$ mm, defined as the inflection point of the initial wall temperature rise of Fig. 4. The heterogeneous fuel conversion rate (Fig. 2) reaches a maximum near the ignition point as the mass transport rates are the highest in the entry and the surface reactions approach their mass-transport limit at ignition. The fuel conversion rate drops downstream of the ignition point because of reduced

TABLE 1

The Elementary Surface Reaction Mechanism

No	Reaction	A [mol, sec, cm]	E_A [kJ/mol]	γ_0 [−]
1	$H_2 + 2\,Pt(s) \rightarrow H(s) + H(s)$			0.046
2	$H(s) + H(s) \rightarrow H_2 + 2\,Pt(s)$	3.7×10^{21}	$67.4 - 6.0^*\Theta_H$	
3	$H + Pt(s) \rightarrow H(s)$			1.0
4	$O_2 + 2\,Pt(s) \rightarrow O(s) + O(s)$			0.07
5	$O(s) + O(s) \rightarrow O_2 + 2\,Pt(s)$	3.7×10^{21}	$213.2 - 60^*\Theta_O$	
6	$O + Pt(s) \rightarrow O(s)$			1.0
7	$H_2O + Pt(s) \rightarrow H_2O(s)$			0.75
8	$H_2O(s) \rightarrow H_2O + Pt(s)$	1.0×10^{13}	40.3	
9	$OH + Pt(s) \rightarrow OH(s)$			1.0
10	$OH(s) \rightarrow OH + Pt(s)$	1.0×10^{13}	192.8	
11	$H(s) + O(s) \Leftrightarrow OH(s) + Pt(s)$	3.7×10^{21}	11.5	
12	$H(s) + OH(s) \Leftrightarrow H_2O(s) + Pt(s)$	3.7×10^{21}	17.4	
13	$OH(s) + OH(s) \Leftrightarrow H_2O(s) + O(s)$	3.7×10^{21}	48.2	
14	$CO + Pt(s) \rightarrow CO(s)$			0.84
15	$CO(s) \rightarrow CO + Pt(s)$	1.0×10^{13}	125.5	
16	$CO_2(s) \rightarrow CO_2 + Pt(s)$	1.0×10^{13}	20.5	
17	$CO(s) + O(s) \rightarrow CO_2(s) + Pt(s)$	3.7×10^{21}	105.0	
18	$CH_4 + 2\,Pt(s) \rightarrow CH_3(s) + H(s)$			0.01
19	$CH_3(s) + Pt(s) \rightarrow CH_2(s) + H(s)$	3.7×10^{21}	20.0	
20	$CH_2(s) + Pt(s) \rightarrow CH(s) + H(s)$	3.7×10^{21}	20.0	
21	$CH(s) + Pt(s) \rightarrow C(s) + H(s)$	3.7×10^{21}	20.0	
22	$C(s) + O(s) \rightarrow CO(s) + Pt(s)$	3.7×10^{21}	62.8	
23	$CO(s) + Pt(s) \rightarrow C(s) + O(s)$	1.0×10^{18}	184.0	

[a](s) denotes surface-bound species. The order of H_2 adsorption is unity with respect to Pt(s), and the order of CO adsorption is 2 with respect to Pt(s). The O_2 sticking coefficient is temperature dependent: $\gamma_{O_2}(T) = 0.07(T_0)/T$ with $T_0 = 300K$.

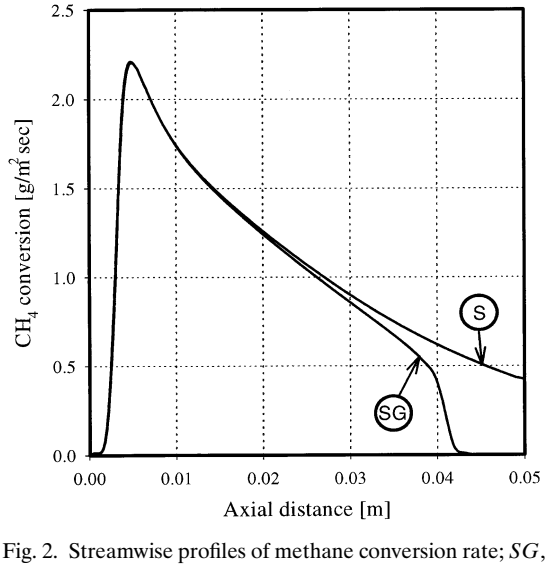

Fig. 2. Streamwise profiles of methane conversion rate; *SG*, gaseous and surface chemistries included; *S*, only surface chemistry included.

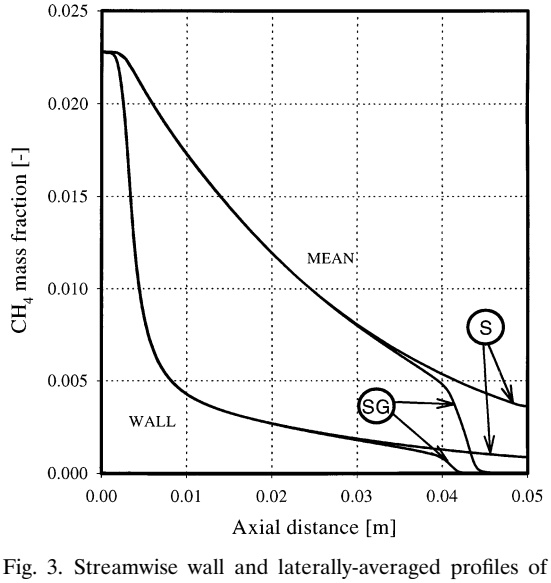

Fig. 3. Streamwise wall and laterally-averaged profiles of CH_4 mass fraction; *SG*, gaseous and surface chemistries included; *S*, only surface chemistry included.

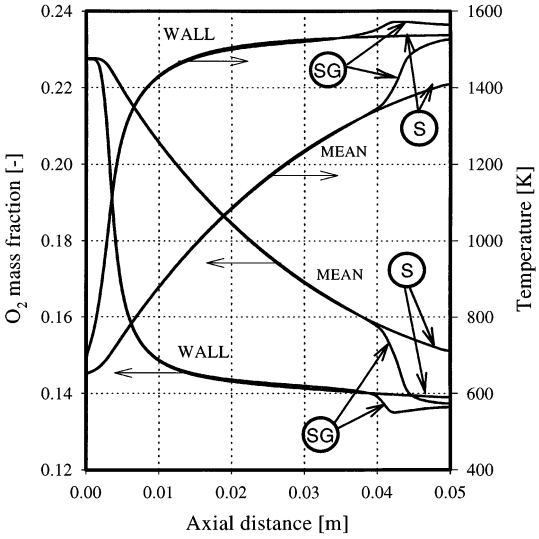

Fig. 4. Streamwise wall and laterally-averaged profiles of temperature and O_2 mass fraction; *SG*, gaseous and surface chemistries included; *S* only surface chemistry included.

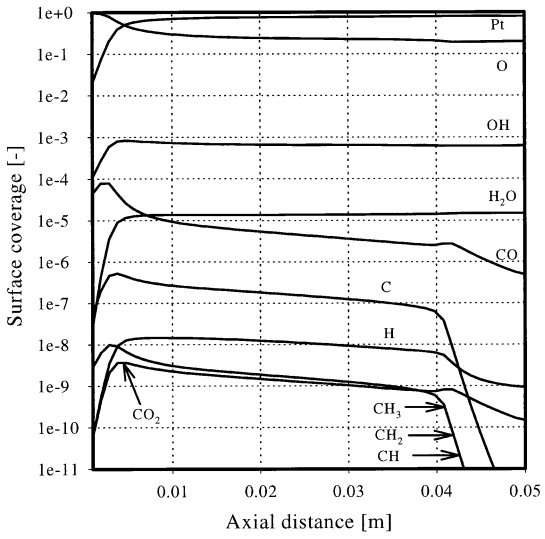

Fig. 5. Streamwise profile of surface coverage for *SG* case.

mass transport rates and upstream fuel depletion. The wall temperatures are the lowest (<800 K) in the initial 1.5 mm. Although heat is transferred via conduction to the initial section, the convective and radiative cooling rates are the highest there. In particular, the importance of radiative heat losses cannot be understated in practical systems where a quick light-off (heterogeneous ignition) is desired. The computations also show that the elliptic fluid mechanical description is important in assessing the precise location of heterogeneous ignition since the streamwise and lateral diffusion are of the same order of magnitude up to $x = 1$ mm.

The surface chemistry before and during heterogeneous ignition can be described with the surface coverage profiles of Fig. 5. Only *SG* profiles are shown since they are identical to the corresponding *S* profiles well downstream of heterogeneous ignition. The wall temperature at the inlet is low (650 K) and the surface is practically covered only with O(s). This is a result of the higher sticking coefficient of O_2 compared to that of CH_4. Further downstream and before ignition, the increase in surface temperature leads to a point where the adsorption/desorption equilibrium of O_2 (reactions R4 and R5 of Table 1, respectively) shifts to desorption, thus releasing free platinum sites onto which CH_4 can adsorb. Reaction flow analysis shows that the CH_x(s) intermediates break down very fast to C(s) and H(s), which then react with the abundant O(s) to create OH(s) and CO(s) that in turn produce H_2O(s) and CO_2(s), which are the major desorbing products. It should be pointed here that other surface reaction mechanisms (see [13]) consider a direct dissociative adsorption of CH_4 to C(s) and H(s), which is consistent with the very fast breakup of the CH_x(s) intermediates of the current scheme. At the heterogeneous ignition location the surface is primarily covered with Pt(s) and O(s) with corresponding coverages of 0.45 and 0.55. For the lean condition of this study the presence of large gas phase wall O_2 concentrations (see Fig. 4) inhibits ignition as higher surface temperatures are required to shift the oxygen adsorption/desorption equilibrium to a point where enough free sites are released. The preheat of the incoming mixture serves to counter this effect and to reduce the heterogeneous ignition distances.

The collapse of the *S* and *SG* profiles shown in Figs. 2 to 4 (at least up to $x = 10$ mm) indicates that the coupling between surface and gas phase reactions is too weak to alter the heterogeneous ignition characteristics. Comparison at ignition between *SG* and *S* shows that gaseous chemistry does not change the wall OH concentration and although it increases the wall

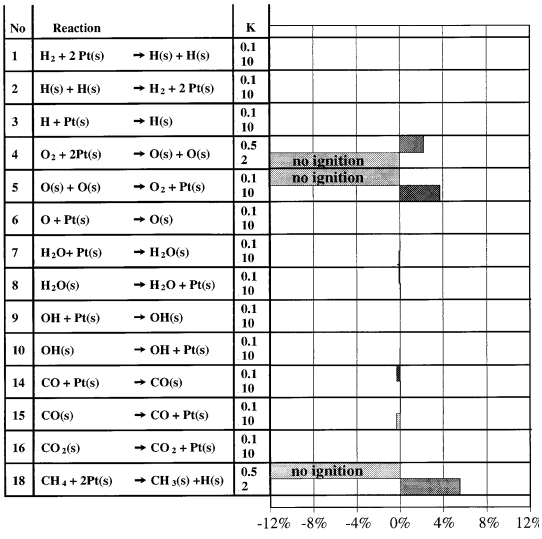

Fig. 6. Sensitivity analysis of surface reactions on heterogeneous ignition (only surface chemistry present); percentage change in heterogeneous fuel conversion for the provided multiplication factors K of each reaction constant.

O and H mass fractions by 2 orders of magnitude, their absolute values are too low ($<10^{-13}$) to influence surface kinetics. Inasmuch as the key steps for ignition are the net adsorption rates of reactants, the above changes in the radical pool do not influence the heterogeneous ignition location.

The last point is also illustrated with the following sensitivity analysis. The pre-exponential constants for each of the 26 surface reactions of Table 1 have been increased/decreased by a factor K and their influence on the total fuel conversion rate (computed at the channel outlet) has been calculated. For the needs of this sensitivity analysis 52 new S simulations were carried out. Reactions involving only surface species are too fast to effect the fuel conversion rate; the rate limiting reactions are the adsorption/desorption reactions and these are shown in Fig. 6. Although Fig. 6 bears the integrated effects over the entire channel, the cases marked "No Ignition" clearly identify the key reactions controlling heterogeneous ignition. The most sensitive reactions are the adsorption of CH_4 and O_2, with positive and negative sensitivities, respectively. Next in importance is the recombinative desorption of O(s) as no ignition takes place with a tenfold decrease in K. The influence of radical adsorption (OH, O, and H) or desorption (OH) is minimal. Reaction flow analysis at the ignition point shows that the major production path for OH(s) is R11f and its major destruction path is the net of reaction R13 (R13f–R13b), each with a rate of about 5.5×10^{-5} moles/cm^{2}sec. The corresponding OH adsorption and desorption rates (R9, R10) are too small (each is about 2×10^{-7} moles/cm^{2}sec) to influence the surface kinetics. Hence the OH(s) coverage as well as the coverage of the other surface species remains unaltered. Similar observations can be made for O(s) and H(s). The O(s) is produced mainly through reactions R4 and R13f and destroyed through R11f and R17, while the H(s) is produced via R18–R21 and destroyed via R11f; the corresponding adsorption reactions R6 and R3 have minimal contributions. The insensitivity to radical adsorption/desorption explains why one-step surface reaction schemes are successful in predicting the heterogeneous ignition location and heterogeneous fuel conversion rates in many technical applications. An additional S simulation was also performed with a global surface step [28] representing the oxidation of CH_4 to CO_2 and H_2O $\dot{r}_{CH_4} = C_{CH_4} A \exp(-E/RT)]$ with $\dot{r}_{CH_4}$ the molar fuel conversion rate per unit area, C_{CH_4} the gas phase fuel concentration at the wall, $A = 1.27 \times 10^3$ m/s, and $E = 77$ kJ/mol. The ignition location was approximately the same and the overall heterogeneous fuel conversion rate was within 1% of the S case with full surface chemistry.

Homogeneous Ignition

The homogeneous ignition as well as the processes leading to it are now discussed. Figures 7 to 13 present lateral profiles at selected streamwise locations of temperature, reactants (CH_4 and O_2), those radicals that participate in the surface mechanism (OH, H, and O), and one major product (H_2O); the lower half (left side) of the channel corresponds to S cases and the upper half (right side) to SG cases. When discussing the lateral wall gradients of Figs. 7SG–13SG, we implicitly reassign the y-axis origin at the wall so that the gradient sign notation is consistent in both S and SG. Figure 2 shows already from $x = 15$ mm a deviation between the S and SG fuel conversion rates,

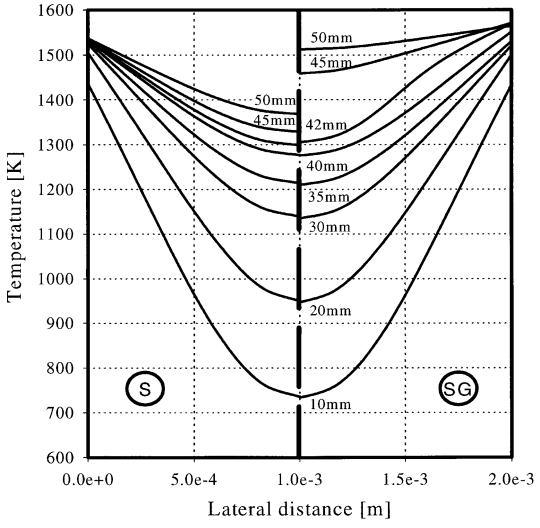

Fig. 7. Lateral temperature profiles at selected streamwise distances; *SG*, gaseous and surface chemistries included; *S* only surface chemistry included.

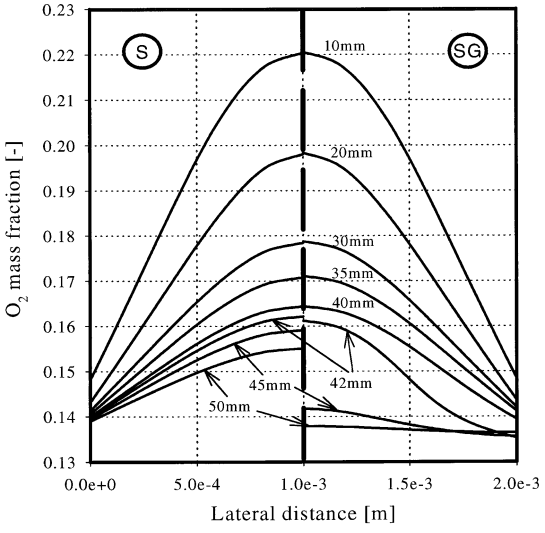

Fig. 9. Lateral O_2 mass fraction profiles at selected streamwise distances; *SG*, gaseous and surface chemistries included; *S*, only surface chemistry included.

which is further increased downstream. This is because in *SG* the fuel breaks down to intermediates whose burnout is contingent upon homogeneous ignition as no adsorption of any other hydrocarbon species is accounted for in the surface mechanism. The homogeneous ignition point can be determined from the drop in the wall fuel conversion rate, wall CH_4, and wall O_2 profiles, or the wall temperature profile rise (Figs. 2–4, *SG*). The inflection point of the wall temperature profile (as well as of the other *SG* wall profiles in Figs. 2–4) is at $x \approx 41$ mm. Such a definition of the homogeneous ignition is consistent with the onset of exothermic gaseous reactions (thermal ignition) as manifested by the sharp rise of the average gas temperature profile at $x \approx 41$ mm (Fig. 4). Other definitions of homogeneous ignition are based on the van't

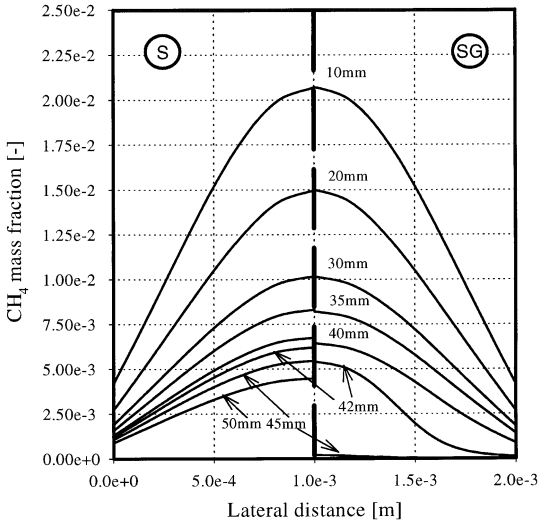

Fig. 8. Lateral CH_4 mass fraction profiles at selected streamwise distances; *SG*, gaseous and surface chemistries included; *S*, only surface chemistry included.

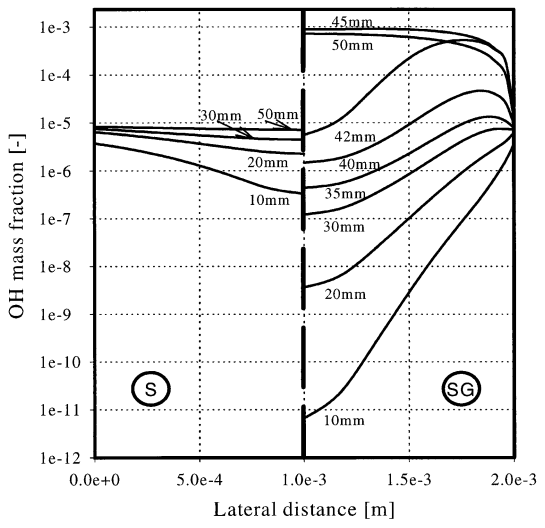

Fig. 10. Lateral OH mass fraction profiles at selected streamwise distances; *SG*, gaseous and surface chemistries included; *S*, only surface chemistry included.

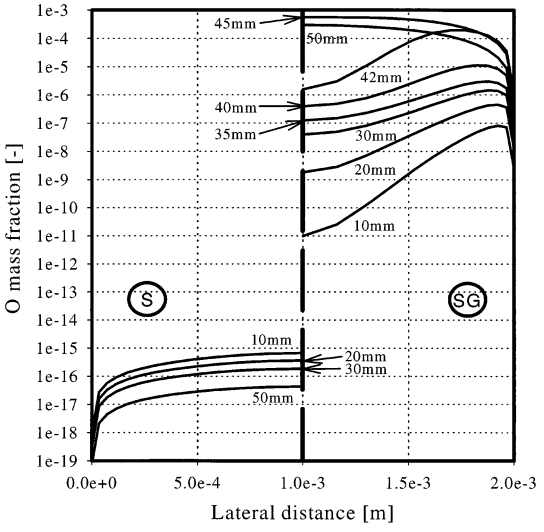

Fig. 11. Lateral O mass fraction profiles at selected streamwise distances; *SG*, gaseous and surface chemistries included; *S*, only surface chemistry included.

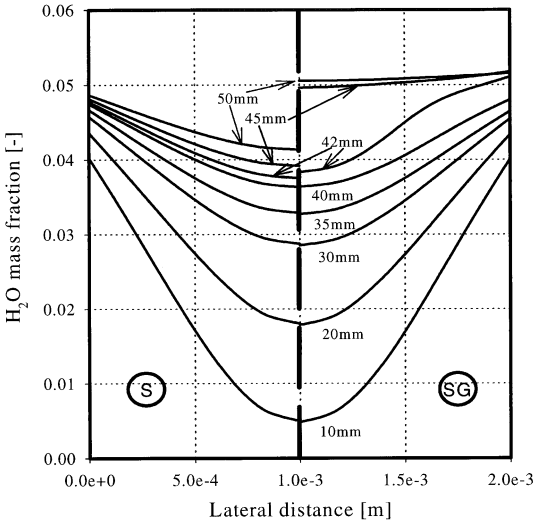

Fig. 13. Lateral H_2O mass fraction profiles at selected streamwise distances; *SG*, gaseous and surface chemistries included; *S*, only surface chemistry included.

Hoff criterion (zero lateral wall temperature gradient) or on the point where the peak of the OH lateral profile moves to the gas phase. The van't Hoff criterion is meaningless in our case as the lateral wall temperature gradients (Fig. 7, *SG*) are negative even after homogeneous ignition. This is a result of heat conduction in the plates and of the small amount of gaseous heat release owing to significant near-wall fuel depletion. In addition, the shift of the OH peak in the gas phase occurs already at $x = 30$ mm (see Fig. 10, *SG*) indicating that gas phase reactions precede any significant gaseous heat release. We have thus opted for the previously described thermal ignition definition. Heterogeneous fuel conversion persists only shortly after homogeneous ignition (up to $x = 42$ mm) and subsequently drops to zero. Gaseous combustion consumes the remaining fuel so that 100% CH_4 conversion is attained at the outlet; 74.5% is heterogeneous and 25.5% is homogeneous.

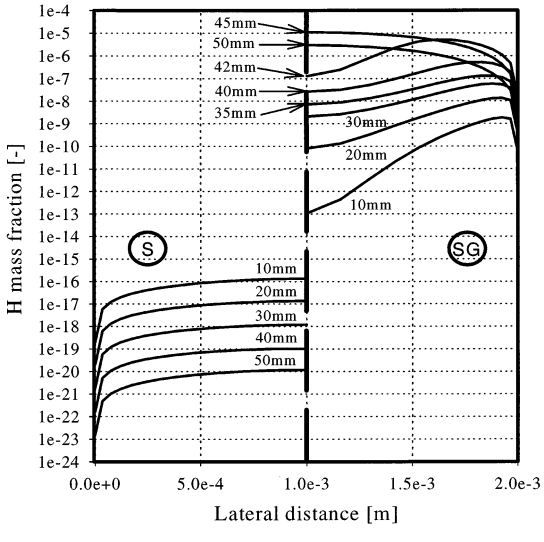

Fig. 12. Lateral H mass fraction profiles at selected streamwise distances; *SG*, gaseous and surface chemistries included; *S*, only surface chemistry included.

The wall gas temperature at $x = 42$ mm (Fig. 4, *SG*) exceeds the adiabatic flame temperature of the mixture (1549 K) by about 23 K due to diffusional imbalance of the limiting reactant. In addition, gas temperatures inside the boundary layer remain superadiabatic at $x = 42$ mm up to 0.1 mm away from the surface. The Lewis number of CH_4 ($\lambda/\rho c_p D_{CH_4}$, with D_{CH_4} the methane diffusivity) is about 0.9, resulting in a higher transport of fuel towards the wall than of heat away from it. Such temperature overshoots could be of importance in technical applications. Superadiabatic wall temperatures are not attained during the predominantly heterogeneous fuel conversion ($x \leq 40$ mm) for two reasons. The first is due to finite rate effects (the surface reactions are not completely mass transport limited, since the wall concentrations of

CH_4 or O_2 are well above zero after heterogeneous ignition as Figs. 3 and 4 indicate) and the second is due to the conduction and radiation heat losses in the catalyst plates.

The build-up of radicals near the homogeneous ignition point is significant, as comparison between the *SG* lateral profiles at $x = 40$ mm and $x = 42$ mm (Figs. 10–12, *SG*) shows. In the preignition period the lateral wall gradient of OH changes from negative (net adsorptive) to positive (net desorptive) as Fig. 10*SG* shows. Such a change has been observed also in the experiments of Griffin et al. [7], who examined the oxidation of lean ($\Phi = 0.55$) methane-air mixtures over Pt-coated surfaces. Accurate prediction of the OH concentrations is crucial in determining the homogeneous ignition point. It must be emphasized that such prediction is possible only with a detailed surface mechanism. The simple one-step surface mechanism with the rate expression given in the end of the heterogeneous ignition section yields a much earlier homogeneous ignition ($x = 31$ mm). To improve over global steps involving only major species, OH desorption is often added to them:

$$CH_4 + (2 + \beta/4)O_2 \rightarrow CO_2 + (2 - \beta/2)\,H_2O + \beta\,OH, \qquad (16)$$

where β is an empirical desorption constant derived usually from comparison with experimentally deduced OH concentrations. Global steps of this type cannot account for the shift in the desorption/adsorption equilibrium of OH before homogeneous ignition. They always impose negative OH wall lateral gradients and in addition they fix the desorption flux of OH relative to that of the major products. Inasmuch as OH is involved in rate limiting gaseous reactions crucial for the onset of homogeneous ignition, which is indeed the case as the following sensitivity analysis shows, such approaches can lead to erroneous interpretations of the ignition processes. The O and H wall lateral profiles (Figs. 11–12, *SG*) are always positive. This is attributed to the absence of O and H desorption in the surface mechanism, justified by the much higher temperatures required to shift the adsorption/desorption equilibria of these radicals to desorption. Furthermore, the flat plate measurements in [7] verify that the O wall gradients are never negative.

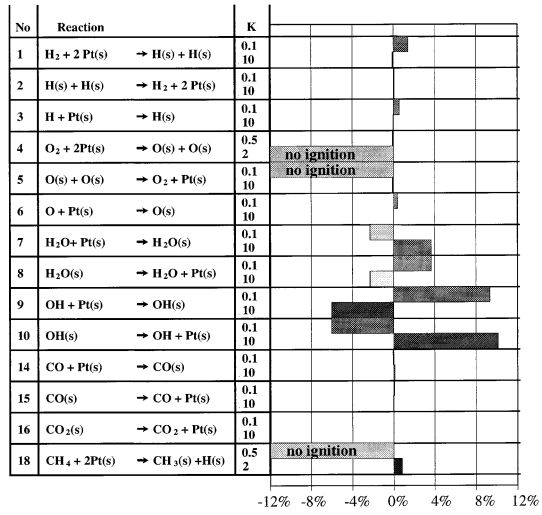

Fig. 14. Sensitivity analysis of surface reactions on homogeneous ignition; percentage change in homogeneous fuel conversion for the provided multiplication factors *K* of each reaction constant.

Between the heterogeneous and homogeneous ignition locations the surface is still covered primarily with Pt(s) and O(s); Pt(s) increases and O(s) decreases with increasing streamwise distance (see Fig. 5). The main reason for this change is the 370K increase in surface temperature between the two ignition points (see Fig. 4). The increase in wall temperature shifts the adsorption/desorption equilibrium of oxygen even further towards desorption, thus releasing free platinum sites. At homogeneous ignition Pt(s) and O(s) have a surface coverage of 0.78 and 0.22, respectively. The surface coverage of carbon-containing species drops between the two ignition points as the fuel flux to the surface is reduced because of upstream depletion.

To understand the key surface reactions influencing homogeneous ignition (apart from the well known inhibiting effect of the near-wall fuel depletion) a sensitivity analysis was performed for the *SG* case. The pre-exponential constants of each surface reaction were increased/decreased in 52 new *SG* simulations. Figure 14 shows the percent change in total homogeneous CH_4 conversion (at the channel exit) for the controlling surface reactions which,

as in the previous S-sensitivity analysis, are the adsorption/desorption heterogeneous reactions. The conditions marked "No Ignition" refer to failure of heterogeneous ignition which was examined before and are not relevant to the homogeneous ignition. It is seen that the OH adsorption/desorption (R9 and R10, respectively) are the most important reactions for gas phase combustion. Detailed study of the ignited SG simulations shows that a tenfold increase (decrease) of the OH desorption factor K moves the homogeneous ignition point to $x \approx 34$ mm ($x \approx 47$ mm) with no influence on the heterogeneous ignition point. The OH(s) coverage does not change with a tenfold increase/decrease in the desorption factor K, for the reasons described in the heterogeneous ignition section. The constancy of OH(s) results, however, in a nearly ten-fold increase/decrease of the OH desorption flux and a corresponding ten-fold increase/decrease of the gaseous OH wall mass fraction; just prior to homogeneous ignition the wall mass fractions of OH for the $K = 1$ (normal), $K = 10$, and $K = 0.1$ cases are 10^{-5}, 10^{-4}, and 10^{-6}, respectively. Similar arguments apply for the OH adsorption, which has an opposite, inhibiting effect.

Next in importance (see Fig. 14) are the H_2O adsorption/desorption reactions (R7 and R8, respectively). The promoting (inhibiting) effect of H_2O adsorption (desorption) however is due to its influence on the OH production route. A ten-fold decrease in the H_2O desorption factor K, for example, leads to a nearly ten-fold increase of the $H_2O(s)$ coverage since the desorption flux of a major product such as H_2O is maintained approximately constant. A ten-fold increase in $H_2O(s)$ coverage leads to nearly three-fold increase in the OH(s) coverage since the $H_2O(s)$ production route passes through OH(s) (reactions R12 and R13). This, in turn, results in a three-fold increase in the OH desorption flux and finally to a three-fold increase in the wall OH mass fraction. The enhanced OH mass fraction is then responsible for the promotion of homogeneous ignition. Finally, as Fig. 14 shows, the adsorption of H_2, H, and O (reactions R1, R3, and R6, respectively) are next in significance and they all inhibit homogeneous ignition. The inhibiting effects decrease in the order of H_2, H, and O adsorption.

The effect of product inhibition on homogeneous ignition was also investigated. The third body efficiency (ω) of H_2O was reduced from its default value of 6.5 to 0.4, i.e., to the corresponding efficiency of N_2 or O_2. This change was applied simultaneously to the eight reversible gas phase reactions of the mechanism [26] that involved enhanced third body efficiencies. A new SG simulation further denoted as $SG(\omega = 0.4)$, showed homogeneous ignition to be delayed by about 4 mm in the $SG(\omega = 0.4)$ compared to the normal SG. Therefore water formation promotes homogeneous ignition. It should be pointed out that studies of hydrogen-air mixtures [6] have shown an opposite, inhibiting effect of H_2O third body efficiency on homogeneous ignition. Comparison of the normal and reduced H_2O efficiency simulations shows that the wall and near wall H radical concentrations are lower in $SG(\omega = 0.4)$ for $x \geq 20$. In the normal SG case, for example, the wall H mass fraction achieves its peak value at the homogeneous ignition point (1.4×10^{-8}), whereas in $SG(\omega = 0.4)$ the peak wall value is lower (10^{-8}) and displaced 4 mm downstream. The O and OH radicals behave similarly, although in $SG(\omega = 0.4)$ the peak wall values are lower than the ones of the normal SG case by only 10% and 3%, respectively. The key reactions with enhanced third body efficiencies, which are responsible for the radical pool change, are

$$HCO + M \rightarrow CO + H + M, \quad \text{(g1)}$$

$$H + O_2 + M \rightarrow HO_2 + M. \quad \text{(g2)}$$

Reaction g1 is a chain propagating reaction, while g2 is a chain terminating reaction, leading to the relatively inactive hydroperoxy radical HO_2. At temperatures below 1200 K, a reduction of the water third body efficiency from 6.5 to 0.4 in reaction g1 has a minimal influence on the H production route because of the relatively high activation energy involved (70.3 kJ/mole). Reaction g2 on the other hand responds quickly to such a reduction in the water efficiency, leading to an overall increase of the H levels. However, at temperatures above 1500 K (which is precisely the range of temperatures encountered at the wall and the near-wall gas for $x \geq 20$) g1 becomes significant for the H production

route; a corresponding reduction of the water third body efficiency in g1 results in a decrease of the H levels that cannot be balanced by the opposing action of g2.

We finally compare the lateral *S* and *SG* profiles of Figs 7–13 up to the point of homogeneous ignition, starting with the OH, O, and H radicals. Although the OH wall mass fractions of Fig. 10 are nearly the same for both *S* and *SG*, the *S* centerline OH concentrations are much higher than the *SG* ones in the initial section ($x \leq 20$ mm). This is because in *SG* the desorbing OH diffuses laterally to the colder channel section where it is destroyed primarily via the fuel breaking reaction

$$CH_4 + OH \rightarrow CH_3 + H_2O \qquad \text{(g3)}$$

and the recombination reaction

$$OH + OH \rightarrow O + H_2O. \qquad \text{(g4)}$$

Figures 11*S* and 12*S* show the O and H concentrations to decrease with increasing x, a result of radical depletion via the adsorption reactions R6 and R3, respectively, and of the absence of any O and H desorption. In *SG*, however, much higher levels of O and H are present due to gaseous reactions; in the initial section O is primarily produced via reaction g4, while H is produced via the attack of intermediates by OH and O radicals, such as

$$CH_3 + OH \rightarrow CH_2O + 2H. \qquad \text{(g5)}$$

The temperature *SG* profiles (Fig. 7) are slightly lower than the corresponding *S* profiles (by as much as 10 K), mainly due to the somewhat smaller heterogeneous fuel conversion in *SG*. The CH_4, O_2, and H_2O profiles show appreciable difference only for $x > 40$ mm.

Homogeneous Gas Phase Combustion

The processes following homogeneous ignition down to the channel exit are now discussed. Figure 2 shows that the heterogeneous fuel conversion ceases at $x \approx 43$ mm, while significant homogeneous fuel conversion has already started at $x \approx 41$ mm. In the region 41 mm $\leq x \leq$ 43 mm both modes of CH_4 conversion are competing, but further downstream homogeneous fuel conversion dominates and at $x \approx 45$ practically all methane has been consumed (average CH_4 mass fraction less than 10^{-5}). The methane *SG* profile (Fig. 8) at the outlet is practically zero, collapsing with the horizontal axis. The gas temperature rises rapidly after homogeneous ignition (Fig. 7, *SG*); its average value at the exit is 1525 K. In addition, the wall temperature decreases from the maximum superadiabatic value of 1572 K attained at $x \approx 42$ mm but it remains superadiabatic down to the channel exit where $T_{W,L} = 1560$ K (see Fig. 4). For $x \geq 42$ mm superadiabatic gas temperatures are also attained in a small zone close to the wall, which decreases in size with increasing x. The wall O_2 profiles (Fig. 4) show a trend opposite to that of the temperature; the wall oxygen mass fraction is a minimum at $x \approx 42$ mm and then increases toward the exit. This behavior is simply another facet of the Lewis number effects.

The profiles in Figs. 10*SG*–12*SG* show substantial increase in the radical pool after homogeneous ignition. Gaseous combustion has already propagated to the channel core at about $x = 45$ mm as the peaks in all lateral radical profiles (and temperature) have moved to the centerline. The maximum values of the H, O, and OH radical concentrations in the entire channel are located at the centerline of $x = 45$ mm, 45.5 mm, and 46 mm, respectively, and they then slowly relax towards their equilibrium values. At the exit the centerline mass fractions of OH, O, and H are 8×10^{-4}, 4×10^{-4}, and 4×10^{-6}, respectively; the corresponding equilibrium values are 5.6×10^{-5}, 1.5×10^{-6}, and 9.9×10^{-10}.

The CO concentrations (not shown) build up through gaseous chemistry well before homogeneous ignition. The *S* and *SG* profiles of CO are nearly the same up to $x \approx 20$ mm, with maximum levels of CO mass fraction of about 7×10^{-5}. Further downstream CO builds up rapidly in *SG* and at $x = 42$ mm has reached a peak value of 6×10^{-3} in a lateral location 0.4 mm away from the wall. After homogeneous ignition CO levels increase and at $x = 45$ mm the peak of CO mass fraction moves to the centerline, with a value 8×10^{-3}. The CO mass fraction drops for $x > 45$ and at the exit its centerline value is 4×10^{-3}, well above the

equilibrium value of 1.1×10^{-6}. The slopes of CO concentration before $x \approx 20$ mm are negative (net desorption) and further downstream are always positive.

The surface after homogeneous ignition and down to the channel outlet is covered mainly with Pt(s) and O(s). The rising wall temperature during homogeneous ignition and down to $x \approx 42$ mm results in further O(s) desorption and rise in Pt(s). For $x > 42$ the wall temperature drops, resulting in a slight recovery of the O(s) coverage. At the exit the Pt(s) coverage is about 0.80 and that of O(s) is about 0.20. The coverage of all carbon containing species decreases (Fig. 5) after homogeneous ignition due to dominant homogeneous fuel conversion. After completion of fuel conversion ($x > 45$ mm) the CH_x(s) and C(s) coverage drop below 10^{-11}.

The zero gradient Neumann outflow conditions for the scalar field are consistent with a frozen chemistry flow. In practical applications, however, homogeneous chemistry continues after the channel exit. Nevertheless, the streamwise rate of change of species concentrations and temperature is very slow near the exit as the lateral SG profiles indicate. This is because the major events, such as fuel consumption and heat release, have been completed well inside the channel. The hydrodynamic field is also well developed as the velocity profiles show, since the increase in gas temperature has an overall effect in reducing the flow Reynolds number which, in turn, reduces the hydrodynamic entry length.

CONCLUSIONS

The catalytically stabilized combustion of a lean ($\Phi = 0.4$) methane-air mixture has been investigated numerically in a laminar plane channel flow configuration consisting of two Pt-coated ceramic plates 50 mm long and 2 mm apart. A two-dimensional elliptic fluid mechanical model with elementary gaseous and surface chemistries was used that included heat conduction in the solid plates and radiative heat transfer from the hot catalyst surfaces. The following are the key conclusions of this study:

1) Heterogeneous ignition takes place about 4 mm after the inlet. Sensitivity analysis of the surface mechanism shows that the key surface reactions influencing heterogeneous ignition are the adsorption of CH_4 (positive sensitivity) and O_2 (negative sensitivity) and the recombinative desorption of O(s) (positive sensitivity). The adsorption or desorption of radicals has no influence on the heterogeneous ignition.

2) Homogeneous ignition takes place at $x \approx 41$ mm. Homogeneous combustion becomes almost immediately the dominant fuel conversion mode, and practically all of the remaining fuel is consumed at $x \approx 45$ mm. Sensitivity analysis shows that the key surface reactions affecting homogeneous ignition are the OH adsorption/desorption with negative/positive sensitivities respectively, and then the H_2O adsorption/desorption again with negative/positive sensitivities, respectively. The H_2O adsorption/desorption importance stems from its direct influence on the OH production path.

3) The effect of product formation on homogeneous ignition was studied by artificially reducing the H_2O third body efficiency in all gaseous reactions with enhanced third body efficiencies. Product formation has a promoting effect on homogeneous ignition due to a shift in the relative importance of the reactions $HCO + M \rightarrow CO + H + M$ and $H + O_2 + M \rightarrow HO_2 + M$, which occurs above 1500 K.

4) Following heterogeneous ignition the surface reactions are never completely mass transport limited but they exhibit finite rate effects. The wall temperature increases with streamwise distance down to the homogeneous ignition point where it achieves a superadiabatic (by 23 K) value due to diffusional imbalance of the limiting (methane) reactant. Further downstream to the channel exit, the wall temperature decreases but remains superadiabatic. Superadiabatic temperatures are also attained in a small zone of the boundary layer near the wall, although the size of this zone decreases after the homogeneous ignition point with increasing streamwise distance.

5) The surface coverage changes significantly with increasing streamwise distance, but Pt(s) and O(s) are always the major surface species. The wall temperature is crucial in determining the ratio Pt(s)/O(s) as it shifts the adsorption/desorption equilibrium of O(s). At the inlet the surface is practically covered with O(s), at het-

erogeneous ignition Pt(s) and O(s) are about 0.45 and 0.55, respectively, at homogeneous ignition the corresponding numbers are 0.78 and 0.22, and finally at the channel exit they are 0.80 and 0.20, respectively.

Support was provided by the Swiss Federal Department of Energy (BEW). We also acknowledge the useful discussions with Prof. H. B. Bockhorn of Karlsruhe University.

REFERENCES

1. Pfefferle, W. C., Bel. Pat. 814,752 (8 November 1974) orig. filing 1971.
2. Hellsing, B., Kasemo, B., and Zhdanov, V. P., *J. Catalysis* 132:210–228 (1991).
3. McCarty, J. G., Proceedings of International Workshop on Catalytic Combustion, Tokyo, Japan, 18–20 April 1994, pp. 108–111.
4. Behrendt, F., Deutschmann, O., Maas, U., Warnatz, J., *J. Vacuum Sci. Technol. A*, 13:1373–1377 (1995).
5. Ikeda, H., Libby, P. A., and Williams, F. A., and Sato, J., *Combust. Flame* 93:138–148 (1993).
6. Bui, P. A., Vlachos, D. G., and Westmoreland, P. R., Twenty-sixth Symposium (Int.) on Combustion, The Combustion Institute, pp. 1763–1770 (1996).
7. Griffin, T. A., Pfefferle, L. D., Dyer, M. J., Crosley, D. R., *Combust. Sci. Technol*. 65:19–37 (1989).
8. Markatou, P., Pfefferle, L. D., Smooke, M. D., *Combust. Sci. Technol*. 79:247–268 (1991).
9. Bruno, C., Walsh, P. M., Santavicca, D. A., Sinha, N., Yaw, Y., and Bracco, F. V., *Combust. Sci. Technol*. 31:43–74 (1983).
10. Buser, S., Benz, P., Schlegel, A., and Bockhorn, H., *Ber. Bunsenges. Phys. Chem*. 97:1719–1723 (1993).
11. Pfefferle, W. C., and Pfefferle, L. D., *Prog. Energy Combust. Sci*. 12:25–41 (1985).
12. Jones, A. F., King-Hele, J. A., Leppington, S. J., *Combust. Sci. Technol*. 95:213–232 (1994).
13. Hickman, D. A., and Schmidt, L. D., "Steps in CH_4 oxidation on Pt and Rh surfaces: High-temperature reactor simulations," *AIChE J*. 39:1164–1177 (1993).
14. Griffin, T., Weisenstein, W., Scherer, V., and Fowles, M., *Combust. Flame* 101:81–90 (1995).
15. Schlegel, A., Buser, S., Benz, P., Bockhorn, H., Mauss, F., Twenty-fifth Symposium (Int.) on Combustion, The Combustion Institute, pp. 1019–1026 (1994).
16. Schlegel, A., Benz, P., Griffin, T., Weisenstein, W., and Bockhorn, H., *Combust. Flame* 105:332–340 (1996).
17. Bond, T. C., Noguchi, R. A., Chou, C-P., Mongia, R. K., Chen, J. Y., and Dibble, R. W., Twenty-sixth Symposium (Int.) on Combustion, The Combustion Institute, pp. 1771–1778 (1996).
18. Kee, R. J., Dixon-Lewis, G., Warnatz, J., Coltrin, M. E., and Miller, J. A., Sandia report SAND86-8246, July 1996 reprint.
19. Coltrin, M. E., Kee, R. J., Rupley, F. M., Sandia report SAND90-8003C, July 1996 reprint.
20. Benz, P., personal communication with R. J. Kee, 1996.
21. Motz, H., and Wise, H., *J. Chem. Phys*. 32:1893–1894 (1960).
22. Deutschmann, O., Behrendt, F., and Warnatz, J., *Catalysis Today* 21:461–470 (1994).
23. Srivatsa, S. K., CHAM TR 201/1, 1977.
24. Schwartz, H. R., *Numerische Mathematic* (in German), B. G. Teuber Publishing Co., Stuttgart, 1988.
25. Incropera, F. P., DeWitt, D. P., *Introduction to Heat Transfer*, Wiley, New York, 1990.
26. Warnatz, J., Maas, U., *Technische Verbrennung* (in German), Springer-Verlag, 1993, pp. 101–102.
27. Warnatz, J., Allendorf, M. D., Kee, R. J., and Coltrin, M. E., *Combust. Flame* 96:393–406 (1994).
28. Snow, G. C., Krill, W. V., Chu, E. K., and Kendall, R. K., Report No. EPA-600/9-84-002, pp. 105–133, 1984.

Received 6 October 1997; revised 26 January 1998; accepted 28 February 1998